Supporting Information

Wu et al. 10.1073/pnas.0911656107

SI Text

SI Materials and Methods. ***Mutant library preparation.*** In general, there are two different ways to target two residues in a protein, simultaneous randomization at both positions, or two separate saturation mutagenesis experiments at the single residue positions. In the latter case, iterative saturation mutagenesis can follow if needed. Inducing cooperative effects between point mutations and, thereby, maximizing the quality of initial mutant libraries becomes possible only when randomizing more than one amino acid position simultaneously, but this entails a pronounced increase in oversampling necessary to ensure, for example, 95% coverage of the relevant protein sequence space (1). This in turn requires a significantly greater screening effort. Assuming the absence of amino acid bias, we have previously calculated for a single amino acid position, applying known algorithms (2, 3), the necessity to screen at least 100 transformants for 95% coverage when using NNK codon degeneracy (N: adenine/cytosine/guanine/thymine; K: guanine/thymine) that encodes all 20 proteinogenic amino acids (1, 4). This number increases to about 3,000 in the case of a randomization site composed of two amino acid positions and to 100,000 when randomizing a three residue site. This analysis is a reminder of the "numbers problem" in directed evolution (1, 4–10) even though focused libraries are involved that, by nature, reduces the relevant protein sequence space. For an efficient process, library quality needs to be maximized, defined in terms of the frequency of hits, and their degree of catalyst improvement and viewed in the light of the screening effort (1). For this purpose, we recently proposed the utilization of reduced amino acid alphabets that, when chosen correctly, lead to mutant libraries of significantly higher quality than that of the conventional NNK libraries (1). For example, when choosing NDT codon degeneracy (D: adenine/thymine: T: thymine) encoding 12 amino acids (Arg, Asn, Asp, Cys, Gly, His, Ile, Leu, Phe, Ser, Tyr, and Val), ≈34 transformants need to be screened for 95% coverage in the case of a single residue site, and only ≈400 in the case of a site comprising two amino acid positions. The NDT-based amino acid alphabet consists of a mix of polar/non-polar, charged/non-charged, and aromatic/non-aromatic representatives that makes it attractive for diverse directed evolution studies including the one at hand.

The libraries and site-specific mutants were constructed by the QuikChange™ PCR method (11) with the template pPAMO and the primers listed below:

Q93NDTP94NDT for 5′-GCGGTACGCTTCCNDTNDTGAGATCCTGCGC-3′

Q93NDTP94NDT rev 5′-GCGCAGGATCTCAHNAHNGGAAGCGTACCGC-3′

Q93NNK for 5′-GCGGTACGCTTCCNNKCCCGAGATCCTGCGC-3′

Q93NNK rev 5′-GCGCAGGATCTCGGGMNNGGAAGCGTACCGC-3′

P94NNK for 5′-GCGGTACGCTTCCCAGNNKGAGATCCTGCGC-3′

P94NNK rev 5′- GCGCAGGATCTCMNNCTGGGAAGCGTACCGC -3′

Q93N for 5′-CGGTACGCTTCCAATCCCGAGATCCTGCGCTAC-3′

Q93N rev 5′-GCGCAGGATCTCGGGATTGGAAGCGTACCGCTC-3′

P94D for 5′-CGGTACGCTTCCCAGGATGAGATCCTGCGCTAC-3′

P94D rev 5′-GCGCAGGATCTCATCCTGGGAAGCGTACCGCTC-3′

The reaction (50 µL final volume) contained: 10 × KOD buffer (5 µL), $MgCl_2$ (2 µL, 25 mM), dNTP (5 µL, 2 mM each), primers (5 µL, 2.5 µM each), template plasmid (2 µL, 10 ng μL^{-1}), and one unit of KOD DNA polymerase. The PCR cycle consisted of an initial denaturation step at 94 °C for 3 min followed by cycling at 94 °C for 1 min, and 72 °C for 14 min for 20 cycles, then a final elongation for 35 min at 72 °C. The template plasmid in 26 µl PCR amplification reaction was removed by digestion with one unit of Dpn I (New England Biolabs) in 3 µL of NEB buffer 4 for 2–3 h at 37 °C. The resulting PCR product was used to transform into electrocompetent *Escherichia coli* TOP10 cells. The cells were spread on LB agar plates containing 100 µg mL^{-1} carbenicilline.

Enzyme expression and purification. The WT PAMO and mutant enzymes were transformed into Escherichia coli TOP 10 cells and grown at 37 °C in LB media with 100 µg mL^{-1} carbenicilline. 2 mL of overnight cultures of WT PAMO and mutants in LB media containing 100 µg mL^{-1} carbenicilline were transferred into 200 mL TB media with 0.1% L-arabinose as inducer and 100 µg mL^{-1} carbenicilline, and incubated at 37 °C with shaking at 250 rpm for 24 h. Cells were harvested by centrifugation and washed once with 0.9% NaCl solution. The cell pellets were resuspended in 10 mL 50 mM Tris-HCl buffer (pH 8.0) and lysed by sonification. The cell debris was removed by centrifugation at $13,000 \times g$ for 30 min at 4 °C. The supernatant was filtered and loaded on a GE Healthcore HisTrapTM FF Crude colummn (5 mL) pre-equilibrated with 50 mM Tris-HCl buffer containing 0.5 M NaCl and 5 mM imidazol. Impurity was removed by imidazol at the concentration of about 25 mM and the enzyme was eluted by 50 mM Tris-HCl buffer with 0.5 M NaCl and 200 mM imidazol. The enzyme fraction was desalted and concentrated by ultrafiltration by using Millipore's Amicon® Ultr-15centrifugal filter devices and then dissolved in 50 mM Tris-HCl buffer (pH 8.0) and stored at −80 °C. The purity of the enzyme was measured by SDS-PAGE. The concentration of the purified enzyme was determined by measuring the absorbance at 441 nm by using an extinction coefficient of 12.4 $mM^{-1}\,cm^{-1}$.

Enzymatic activity assay. The activities of the purified enzymes were determined spectrophotometrically by monitoring the decrease in the level of NADPH over time at 25 °C and 340 nm ($\varepsilon340 = 6.22\ mM^{-1}\,cm^{-1}$). 1.0 mL reaction mixture contained 50 mM Tris-HCl (pH 8.0), 100 µM NADPH, 2 mM substrate (added as a concentrated solution in acetonitrile), 1 µM purified enzyme. One unit of activity was defined as the amount of enzyme required to consume 1 µmol of NADPH per min. For measuring the thermostability of the WT PAMO and mutants, solutions of the purified enzymes (about 30 µM) were incubated at 50, 55, 57, and 60 °C for 1 h. The residual activity was determined as described above in the presence of 2 mM phenylacetone.

Starting substrates (ketones) and products (lactones). Ketones *rac*-**1f**, **1h**, and **1i** were prepared by alkylation as described. Ketone *rac*-**1b** was prepared by the reported method, and the others purchased from Sigma–Aldrich, Acros, TGI, and Fluka (used without further purification). The racemic lactones were prepared by conventional BV-oxidation of the corresponding ketones by using *m*-chloroperoxybenzoic acid (mCPBA). All of the synthesized compounds were isolated by silica gel chromatography and identified by ^{1}H and ^{13}C NMR spectroscopy.

Identification of products from biotransformation. After extraction as described above, the ketones and lactones were identified by comparison of their retention times on GC (HP-5 and the corresponding chiral separation columns) with authentic racemic compounds.

Determination of the enantiomeric excess of residual ketones and produced lactones. The *ee*-values of residual ketones **1** and lactones **2** were determined by chiral GC directly. The absolute configurations were made by comparison with authentic samples and referring to the literature, the respective lactones being prepared by using the recombinant CHMO from *Acinetobacter* sp. NCIMB 9871 (12–14) as a catalyst in the reaction of ketones **1c**–**1h** and **1k**, and P3-PAMO mutant (15) for preparing **2a** and **2j**. The (tentative) assignment of the absolute configuration of lactone **2b** and **2i** was made on the basis of analogy.

Induced fit molecular docking. The ligand phenylacetone was treated by using the procedure LigPrep equipped with the Maestro 8.5 (Schrödinger, LLC) (16). OPLS_2005 force field was utilized to optimize the geometry and minimize the energy. WT PAMO crystal structure (PDB code: 1w4x) was optimized by the Protein Preparation Wizard, available tool in the Maestro 8.5 interface program. The missing hydrogen atoms were added, bond orders and formal charges were adjusted, and all the water molecules were removed. After hydrogen bonds were optimized, the obtained structure was further subjected to minimize the energy with the OPLS_2005 force field as implemented in Macromodel 9.6 (Schrödinger, LLC) (17).

The induced fit docking studies were performed by using the Induced Fit Docking (18) protocol implemented in Maestro 8.5. The center of the Glide enclosing box was the centroid of residues Arg337, Gln152, Leu153, Ala442, and Trp501 based on the catalytic mechanism of PAMO. In the first step of Glide ligand docking, Arg337 was chosen to temporarily remove the side chains and replaced with Ala. The Coulomb-vdW scaling factors were changed to the default values of 0.7 and 0.5 for the protein and ligand, respectively. A maximum of 20 poses were retained. In the second phase of docking, the Prime application reversed the temporary replacement of Arg 337 with Ala, refined nearby residues, and optimized side chains. In the final docking phase, the ligand was redocked into all induced fit protein structures that were within 30 kcal/mol of the lowest energy structure by using the Glide SP scoring function (19). A maximum of 20 poses were needed. Each was ranked by using the composite induced fit score. Each pose was further analyzed manually to determine the substrate binding mode, the distance between the flavin C4a atom and the oxygen atom of the ligand. The best induced fit docking parameters were as follows: docking score $= -5.05$ kcal/mol, IDFScore $= -1355.9$ kcal/mol, and prime energy $= -27018.2$ kcal/mol. The distance between the oxygen atom of phenylacetone and C4a atom of FAD was 6.64 Å.

Molecular dynamics (MD) simulations. Using the published X-ray structural data of 1W4X, the in silico structure determinations of the wild type and mutants were performed with the Schrödinger software package (16). Polak-Ribier Conjugate Gradient with a convergence threshold on the gradient of 0.05 kJ/Å/mol was used for the minimization of the structures of wild type (WT) and also used to minimize the structure after mutations (17). These first modeled structures included FAD molecule, but not NADP$^+$. The selected force field for these calculations was OPLS_2005, and the surface area-based version of the generalized born (GB/SA) model was used for treatment of solvent (water), and its dielectric constant was assigned a value of one. To generate the solvated systems for dynamic simulations, a cubic periodic unit cell containing 71484 water molecules, 133 Na$^+$ ions, and 133 Cl$^-$ ions was used. This solvent cube was defined by adding a minimum layer of 20 Å buffer molecules from the protein surface, having 0.15 M NaCl. All simulations used the SPC water model (20, 21), and the OPLS-AA force field for protein. Long-range electrostatic interactions using Particle Mesh Ewald (PME) and van der Waals interactions were computed with a real space contributions truncated at 9 Å. Bond lengths to hydrogens were constrained by using SHAKE algorithm. We used a RESPA integrator with time steps set to 2 fs for bonded and short-range nonbonded interactions, and six to fs for long-range electrostatic interactions. Before every dynamic simulation, the solvated systems were relaxed into a local energy minimum using 50 steps of a hybrid method of steepest descent minimization and a limited-memory Broyden-Fletcher-Goldfarb-Shanno (L-BFGS) minimization. Additionally, the model systems were relaxed before simulation through a series of minimization and short dynamic simulations (NPT ensemble using a Berendsen thermostat and barostat) equilibrating the system at 300 K and 1 bar. Finally, production simulations were performed for every solvated system during 2 ηs, coupling the system using NPT simulation, maintaining 1 Atm at 300 K with a Martyna–Tobias–Klein barostat (relaxation time of 2 ρs) and a Nose–Hoover thermostat (relaxation time of 0.5 ρs). MD simulations were performed with the Desmond program by using an algorithm for high-speed parallel execution (22–27), recording conformations every 1.2 ρs. After the first production simulation NADPH molecule was included in the final structure using homology positioning by using structural alignment with the crystal structure of cyclohexanone monooxygenase (CHMO); PDB ID: 3GWD. Finally, second production simulations of the wild type and double mutant Gln93Asn/Pro94Asp were performed including FAD and NADP$^+$ in the structure by using the same MD simulation procedure described above. The second MD simulations were run for 6 ns recording conformations every 1.2 ρs.

Analysis of MD simulations. The dynamics trajectories were analyzed by using the Schrödinger software package (16), VMD software (28), and Microsoft Excel. Protein structure superpositons were performed using FAD molecule and residues 22, 23, 25, 26, 27, 46, 47, 52, 53, 54, 57, 64, 66, 118, 119, 149, 150, 151, 395, 399, and 450 as anchor).

Construction of covariance maps. The technique of covariance maps constitutes a useful tool in the elucidation of motions occurring in enzymes and their effects on catalysis, specifically in the identification of regions or domains whose movements are correlated or anti-correlated (29–33). Indeed, a referee suggested that this be done in the present study. As shown here, such an analysis not only corroborates our mechanistic and structural conclusions, it also becomes clear that the technique can be helpful in choosing appropriate mutagenesis sights that might lead to allostery (that we should have applied in the first place). Using GROMACS tools for covariance matrix calculation (http://www.gromacs.org/), and the *R* statistical package for correlation maps and plots generation (http://www.r-project.org/), cross-correlation coefficients of the C_α atoms of the residues were derived by using 6 ns simulations of WT PAMO and of the superior double mutant Gln93Asn/Pro94Asp, in both cases including FAD and NADP$^+$ in the respective binding domains. Fig. S5 shows the results of WT PAMO that indicate inter alia and high correlation values between the interface FAD-NADP domains. It can be seen that significant movement correlation exists between the loop segment Trp177-Glu180 (NADP-binding domain) the loop segment Tyr56-Tyr60 (FAD-binding domain) and the N-terminal region

(Ala91-Glu95) of the α-helix. Correlation with active site residues are observed. This finding supports our original conclusion regarding the appropriate choice of the saturation mutagenesis site that could lead to the reshaping of the binding pocket. In contrast, the interface helix-NADP domains do not appear to show significant correlations with remote regions that can in principle be used as a basis for discarding such sites for mutagenesis. Moreover, it can be seen that the loop segments Trp177-Glu180 (NADP-binding domain) and Tyr56-Tyr60 (FAD-binding domain) are already well correlated, suggesting that any further attractive interactions are not likely to cause significant structural changes. The N-terminal region of the α-helix (Ala91-Glu95) appears to be a more suitable option, because it is localized in the most stable region of WT PAMO according to the RMSD values, and in close contact with loop segment Tyr56-Tyr60 (FAD-binding domain). To analyze the superior double mutant Gln93Asn/Pro94Asp, the same procedure was applied (Fig. S6). One important conclusion readily made is that increased correlation exists between the mutation site 93/94 and the FAD segment in the interface FAD-NADP domains, indicating increased contact as originally suspected and likewise indicated by the MS simulations themselves. Finally, comparing the differences in the covariance maps illuminates structural differences particularly around the residues around the binding pocket, hinges and the NADP-binding domain (Fig. S7). These differences in correlated movements of particular segments in the enzyme probably respond to the new conformations induced by the specific mutational changes. Domains are displaced from the original position, creating a new environment at the binding pocket.

1. Reetz MT, Kahakeaw D, Lohmer R (2008) Addressing the numbers problem in directed evolution. *ChemBioChem* 9:1797–1804.
2. Mena MA, Daugherty PS (2005) Automated design of degenerate codon libraries. *Protein Eng, Des Sel* 18:559–561.
3. Bosley AD, Ostermeier M (2005) Mathematical expressions useful in the construction, description and evaluation of protein libraries. *Biomol Eng* 22:57–61.
4. Reetz MT, Kahakeaw D, Sanchis J (2009) Shedding light on the efficacy of laboratory evolution based on iterative saturation mutagenesis. *Mol BioSyst* 5:115–122.
5. Lutz S, Bornscheuer UT (2009) *Protein Engineering Handbook* (Wiley-VCH, Weinheim).
6. Turner NJ (2009) Directed evolution drives the next generation of biocatalysts. *Nat Chem Biol* 5:567–573.
7. Jäckel C, Kast P, Hilvert D (2008) Protein design by directed evolution. *Annu Rev Biophys Biomol Struct* 37:153–173.
8. Bershtein S, Tawfik DS (2008) Advances in laboratory evolution of enzymes. *Curr Opin Chem Biol* 12:151–158.
9. Reetz MT (2008) Directed evolution as a means to engineer enantioselective enzymes. In *Asymmetric Organic Synthesis with Enzymes*, eds. Gotor V, Alfonso I, Garcia-Urdiales E (Wiley-VCH, Weinheim).
10. Reetz MT, Carballeira JD (2007) Iterative saturation mutagenesis (ISM) for rapid directed evolution of functional enzymes. *Nat Protoc* 2:891–903.
11. Hogrefe HH, Cline J, Youngblood GL, Allen RM (2002) Creating randomized amino acid libraries with the QuikChange® multi site-directed mutagenesis kit. *BioTechniques* 33:1158–1165.
12. Kayser MM (2009) 'Designer reagents' recombinant microorganisms: New and powerful tools for organic synthesis. *Tetrahedron* 65:947–974.
13. Stewart JD (1998) Cyclohexanone monooxygenase: A useful reagent for asymmetric Baeyer–Villiger reactions. *Curr Org Chem* 2:195–216.
14. Mihovilovic MD (2006) Enzyme mediated Baeyer–Villiger oxidations. *Curr Org Chem* 10:1265–1287.
15. Bocola M, Schulz F, Leca F, Vogel A, Fraaije MW, Reetz MT (2005) Converting phenylacetone monooxygenase into phenylcyclohexanone monooxygenase by rational design: Towards practical Baeyer–Villiger monooxygenases. *Adv Synth Catal* 347:979–986.
16. Schrödinger, LLC (2008) Maestro 8.5 user manual, Schrödinger Press (New York, NY).
17. Mohamadi NGJ, Richards WC, Guida R, Liskamp M, Lipton C, Caufield G, Chang T, Hendrickson WC, Still WC (1990) Macromodel—an integrated software system for modeling organic and bioorganic molecules using molecular mechanics. *J Comput Chem* 11:440–467.
18. Sherman W, Day T, Jacobson MP, Friesner RA, Farid R (2006) Novel procedure for modeling ligand/receptor induced fit effects. *J Med Chem* 49:534–553.
19. Friesner RA, Banks JL, Murphy RB, Halgren TA, Klicic JJ, Mainz DT, Repasky MP, Knoll EH, Shelley M, Perry JK, Shaw DE, Francis P, Shenkin PS (2004) Glide: A new approach for rapid, accurate docking and scoring. 1. Method and assessment of docking accuracy. *J Med Chem* 47:1739–1749.
20. Berendsen HJC, Postma JPM, van Gunsteren WF, Hermans J (1981) in *Intermolecular Forces*, ed Pullmann B (Reidel, Dordrecht), p 331.
21. Berweger CD, van Gunsteren WF, Müller-Plathe F (1995) Force field parametrization by weak coupling. Re-engineering SPC water. *Chem Phys Lett* 232:429–436.
22. Bowers KJ, Chow E, Xu H, Dror RO, Eastwood MP, Gregersen BA, Klepeis JL, Kolossváry I, Moraes MA, Sacerdoti FD, Salmon JK, Shan Y, Shaw DE (2006) Scalable algorithms for molecular dynamics simulations on commodity clusters. *Proceedings of the ACM/IEEE Conference on Supercomputing (SC06)*, Tampa, Florida.
23. Cerutti DS, Duke R, Freddolino PL, Fan H, Lybrand TP (2008) Vulnerability in popular molecular dynamics packages concerning Langevin and Andersen dynamics. *J Chem Theory Comput* 4:1669–1680.
24. Arkin IT, Xu H, Jensen MØ, Arbely E, Bennett ER, Bowers KJ, Chow E, Dror RO, Eastwood MP, Flitman-Tene R, Gregersen BA, Klepeis JL, Kolossváry I, Shan Y, Shaw DE (2007) Mechanism of Na^+/H^+ antiporting. *Science* 317:799–803.
25. Shaw DE (2005) A fast, scalable method for the parallel evaluation of distance-limited pairwise particle interactions. *J Comput Chem* 26:1318–1328.
26. Bowers KJ, Dror RO, Shaw DE (2007) Zonal methods for the parallel execution of range-limited N-body simulations. *J Comput Phys* 221:303–329.
27. Bowers KJ, Dror RO (2006) The midpoint method for parallelization of particle simulations. *J Chem Phys* 124:184109.
28. Humphrey W, Dalke A, Schulten K (1996) VMD: Visual molecular dynamics. *J Mol Graphics Modell* 14:33–38.
29. Ichiye T, Karplus M (1991) Collective motions in proteins: A covariance analysis of atomic fluctuations in molecular dynamics and normal mode simulations. *Proteins: Struct Func Genet* 11:205–217.
30. Liu J, Nussinov R (2008) Allosteric effects in the marginally stable von Hippel-Lindau tumor suppressor protein and allostery-based rescue mutant design. *P Nat Acad Sci USA* 105:901–906.
31. Hammes-Schiffer S, Benkovic SJ (2006) Relating protein motion to catalysis. *Annu Rev Biochem* 75:519–541.
32. Radkiewicz JL, Brooks III CL (2000) Protein dynamics in enzymatic catalysis: Exploration of dihydrofolate reductase. *J Am Chem Soc* 122:225–231.
33. Ivanov I, Chapados BR, McCammon JA, Tainer JA (2006) Proliferating cell nuclear antigen loaded onto double-stranded DNA: Dynamics, minor groove interactions and functional implications. *Nucleic Acids Res* 34:6023–6033.

Table S1. Distances between pars of amino acids in the active pocket of the average protein structures of WT PAMO, mutant Pro94Asp and mutant Gln93Asn/Pro94Asp. Average distances between the Cα of binding pocket residues were calculated by using the conformers in the final 1 ns of the MD simulation. Productive MD simulations were run during 2 ns, including coenzyme FAD.

		WT PAMO	Mutant Pro94Asp	Mutant Gln93Asn/Pro94Asp
	Amino acids	Aver. dist Cα-Cα (Å)*	Aver.dist Cα-Cα (Å)*	Aver. dist Cα-Cα (Å)*
A	Ser196-Lys336	11.5 ± 0.3	11.4 ± 0.3	12.1 ± 0.3
B	Ser196-Phe389	7.6 ± 0.4	8.6 ± 0.3	10.9 ± 0.4
C	Lys336-Phe389	11.5 ± 0.4	12.6 ± 0.4	13.5 ± 0.4
D	Lys336-Trp501	8.8 ± 0.3	8.4 ± 0.3	9.4 ± 0.2
E	Phe389-Trp501	12.5 ± 0.4	12.4 ± 0.4	13.7 ± 0.3
F	Trp501-Leu153	12.8 ± 0.3	12.6 ± 0.3	13.8 ± 0.4

*± Standard deviation.

Table S2. Distances between pars of amino acids in the active pocket of the average protein structure of WT PAMO, and mutant Gln93Asn/Pro94Asp. Average distances between the Cα of binding pocket residues were calculated by using the conformers in the final 1 ns of the MD simulation. Productive MD simulations were run during 6 ns including coenzymes FAD and NADP$^+$.

		WT PAMO	Mutant Gln93Asn/Pro94Asp
	Amino acids	Aver. dist Cα-Cα (Å)*	Aver. dist Cα-Cα (Å)*
A	Ser196-Lys336	12.3 ± 0.3	11.4 ± 0.3
B	Ser196-Phe389	9.3 ± 0.2	10.3 ± 0.4
C	Lys336-Phe389	13.3 ± 0.3	14.3 ± 0.3
D	Lys336-Trp501	8.7 ± 0.2	9.4 ± 0.2
E	Phe389-Trp501	13.8 ± 0.4	14.4 ± 0.3
F	Trp501-Leu153	13.7 ± 0.4	14.8 ± 0.3

*± Standard deviation.

Table S3. Backbone shift between WT PAMO and mutant Gln93Asn/Pro94Asp for residues forming the active pocket. WT PAMO (*Green*) and mutant Gln93Asn/Pro94Asp (*Blue*) structural conformers of the MD simulation were previously superposed by using the FAD molecule and FAD-binding residues. Distance results represent the displacement of the Cα residues between WT and mutant PAMO related with the position of the FAD molecule in the enzyme. The distances between the Cα of residues and the atom C4A of the flavin ring were also included together with a diagram of the kind of measurement presented in this table.

	WT PAMO//Mutant Gln93Asn/Pro94Asp	WT PAMO	Mutant Gln93Asn/Pro94Asp
Amino acid	Aver. dist Cα-Cα (Å)*	Aver. dist Cα-C$_{4A}$ (Å)*	Aver. dist Cα-C$_{4A}$ (Å)*
Gln152	1.0 ± 0.3	10.5 ± 0.3	11.4 ± 0.3
Leu153	1.1 ± 0.2	10.8 ± 0.4	10.3 ± 0.3
Ser154	1.0 ± 0.3	13.7 ± 0.3	12.2 ± 0.3
Ser196	3.0 ± 0.4	9.8 ± 0.2	10.5 ± 0.3
Lys336	4.4 ± 0.5	14.8 ± 0.3	13.0 ± 0.3
Arg337	3.7 ± 0.4	11.3 ± 0.3	9.6 ± 0.3
Phe389	1.2 ± 0.3	13.8 ± 0.3	13.6 ± 0.4
Asp390	0.9 ± 0.3	15.5 ± 0.3	15.0 ± 0.3
Ala391	3.3 ± 0.3	14.5 ± 0.3	14.5 ± 0.4
Leu392	6.3 ± 0.3	17.7 ± 0.4	13.2 ± 0.3
Ser441	1.8 ± 0.5	11.6 ± 0.3	11.3 ± 0.3
Ala442	2.7 ± 0.3	9.8 ± 0.3	8.6 ± 0.3
Met446	0.7 ± 0.2	7.3 ± 0.2	7.3 ± 0.2
Trp501	2.9 ± 0.5	19.3 ± 0.4	18.6 ± 0.4
Thr503	2.8 ± 0.5	22.5 ± 0.5	22.3 ± 0.5
Met515	2.3 ± 0.5	19.4 ± 0.3	18.7 ± 0.3
Leu516	2.3 ± 0.5	17.7 ± 0.3	17.1 ± 0.3

*± Standard deviation.

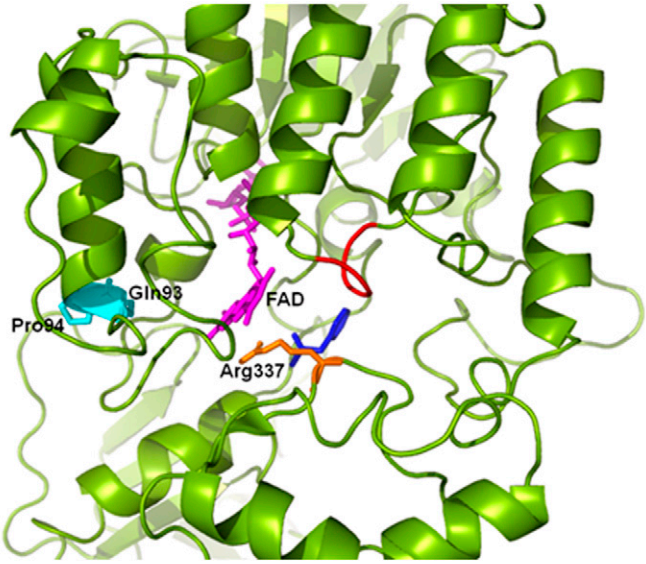

Fig. S1. Excerpt of the X-ray structure of PAMO showing the chosen two-residue randomization site Gln93/Pro94 (*Cyan*), FAD (*Magenta*), Arg337 (*Orange*), phenylacetone (*Gray*), and loop (*Red*) targeted in previous mutagenesis studies.

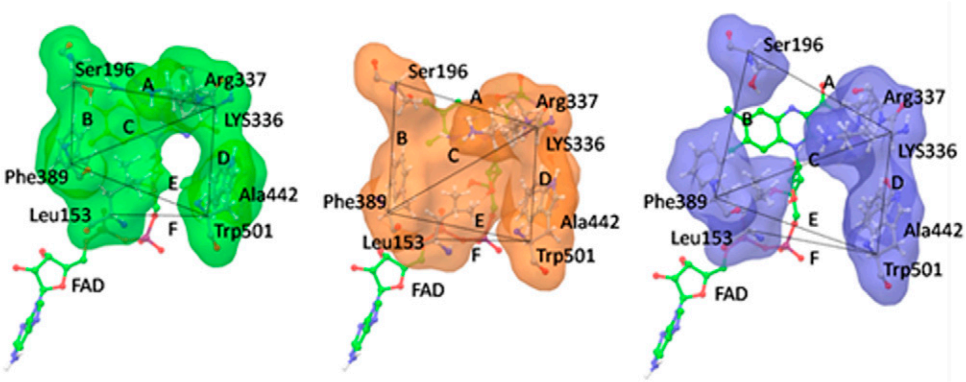

Fig. S2. Comparison of WT PAMO (*Green*), mutant Pro94Asp (*Orange*), and mutant Gln93Asn/Pro94Asp (*Blue*) binding pocket conformations. Binding pocket diagrams include some of the closest FAD related amino acids of the binding pocket and distance measurements amongst them. Value distances are shown in the Table S1 with their corresponding letter in the figure. The binding pocket surface and diagrams were obtained from the average structure of 1 ns of MD trajectory after 1 ns of equilibration. Productive MD simulations were run during 2 ns including coenzyme FAD.

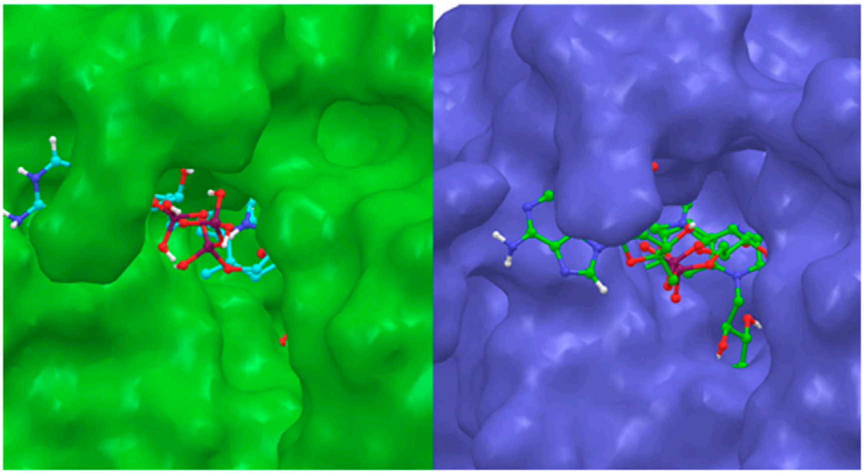

Fig. S3. Surface construction of the binding pocket in WT PAMO (*Green*) and mutant Gln93Asn/Pro94Asp (*Blue*). Average structures were obtained from the conformers of 1 ns of MD trajectory after 5 ns of equilibration. Productive MD simulations were run during 6 ns including coenzyme FAD and $NADP^+$.

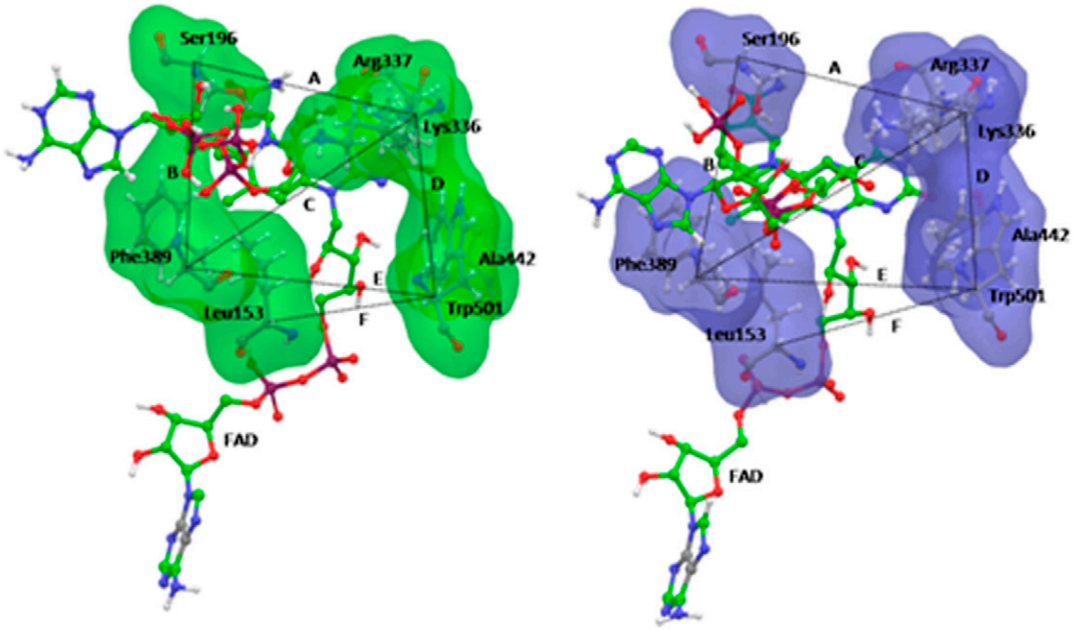

Fig. S4. Comparison of WT PAMO (*Green*) and mutant Gln93Asn/Pro94Asp (*Blue*) binding pocket conformation. In these diagrams are included some of the closest FAD related amino acids of the binding pocket and distance measurements amongst them. Value distances are shown in the Table S2 with their corresponding letter in the figure. The binding pocket diagrams were obtained from the average structure of 1 ns of MD trajectory after 5 ns of equilibration. Productive MD simulations were run during 6 ns including coenzyme FAD and NADP$^+$.

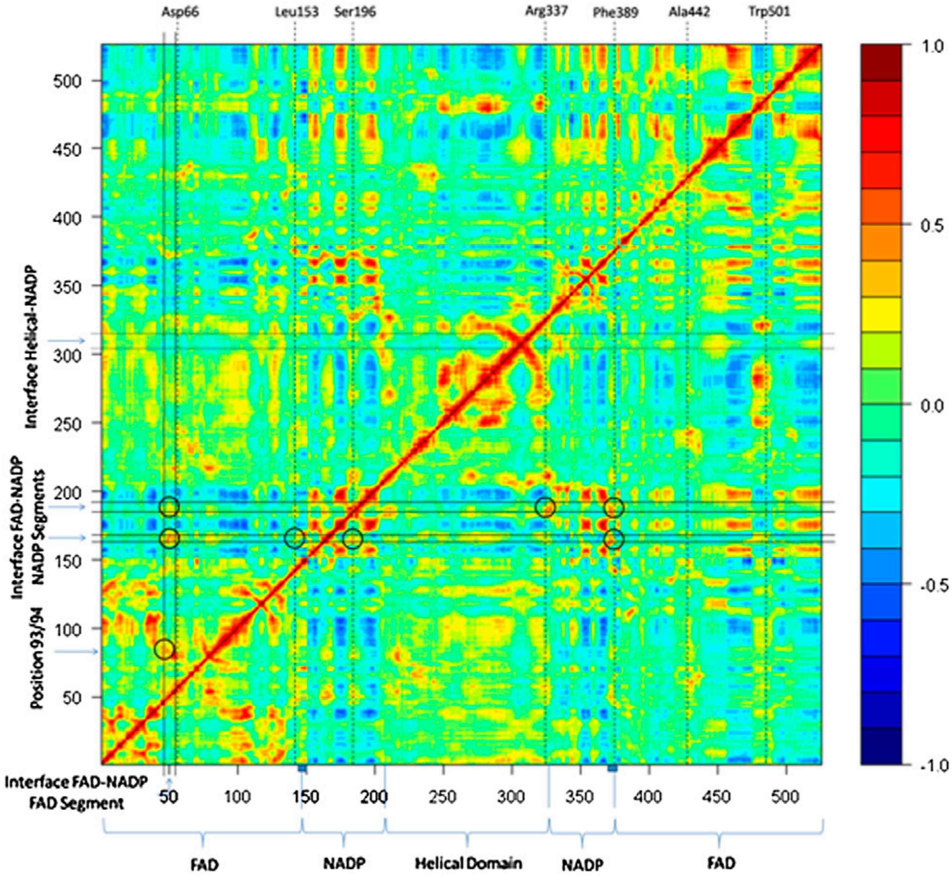

Fig. S5. Covariance map of WT PAMO (with FAD and NADP$^+$), featuring correlated and anti-correlated motions. Positive correlations in descending order are shown in *Red*, *Orange*, and *Yellow*. *Light Green* corresponds to non-correlated regions, and anti-correlated motions are shown in *Cyan* and *Blue*. Residue segments corresponding to the different domains are marked, and the regions between the *Solid Lines* localize the inter-domain interface. Residues forming the binding pocket are indicated with *Dashed Lines*. Hinge regions between the NADP- and FAD-binding domains are shown with a *Blue Square* below the x-axis. *Circles* show high correlation values between the interface NADP-FAD domains and the binding pocket.

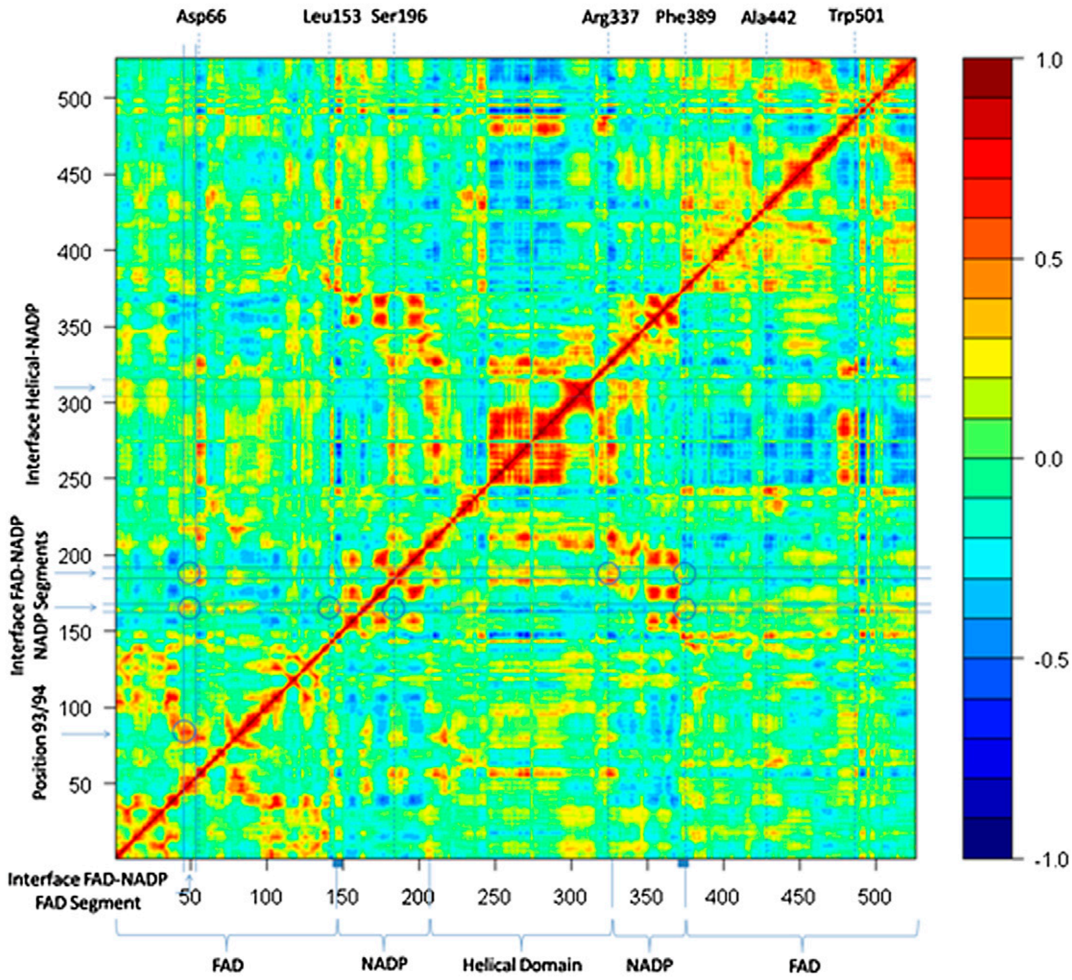

Fig. S6. Covariance map of the superior double mutant Gln93Asn/Pro94Asp (with FAD and NADP$^+$), featuring correlated and anti-correlated motions. Positive correlations in descending order are shown in *Red*, *Orange*, and *Yellow*. *Light Green* corresponds to non-correlated regions. Anti-correlated motions are shown in *Cyan* and *Blue*. Residue segments corresponding to the different domains are marked, and the regions between the *Solid Lines* localize the inter-domain interface. Residues forming the binding pocket are indicated with *Dashed Lines*. Hinge regions between the NADP- and FAD-binding domains are shown with a *Blue Square* below the x-axis. *Circles* show the regions of high correlation values between the interface NADP-FAD domains and the binding pocket observed in the correlation map of WT PAMO.

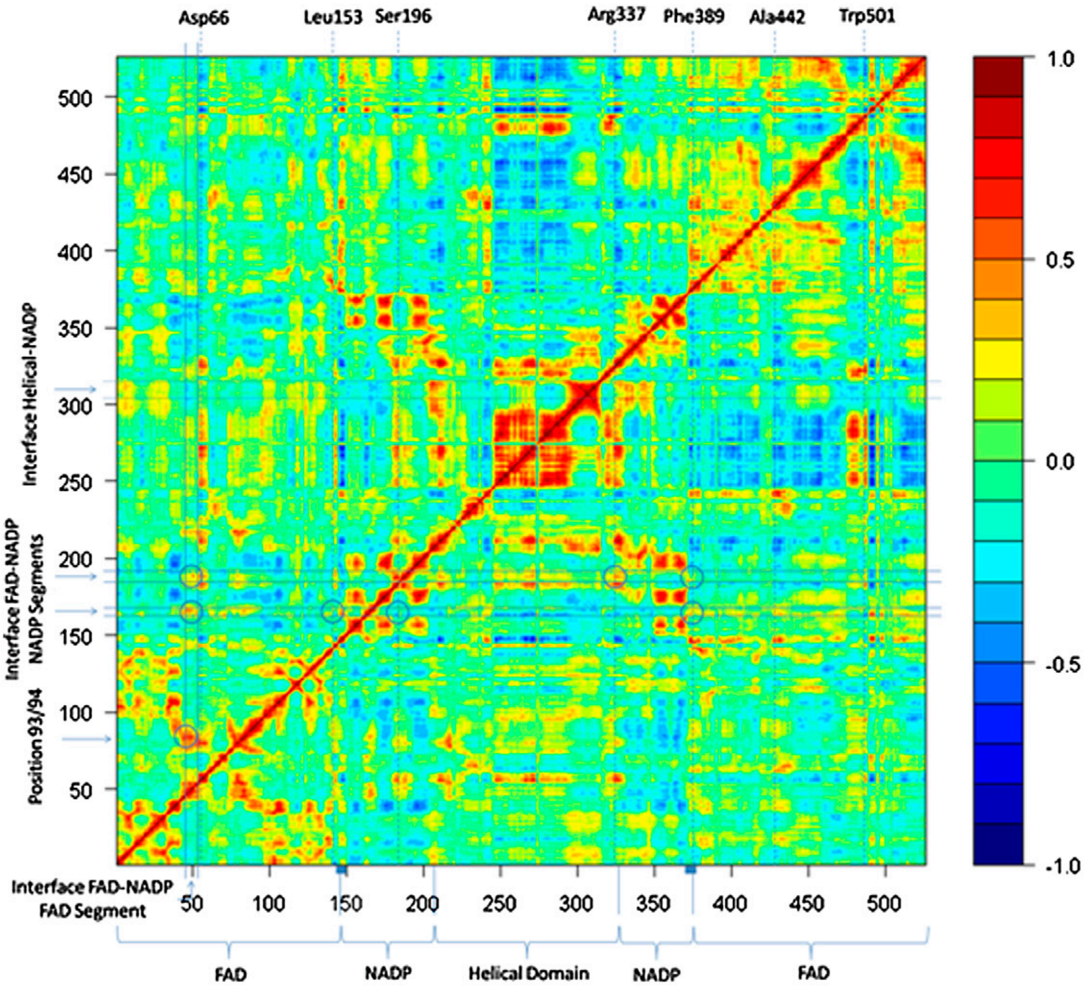

Fig. S7. Cross-correlation coefficient differences between WT PAMO and the superior double mutant Gln93Asn/Pro94Asp. Residue segments corresponding to the different domains are marked, and the regions between the *Solid Lines* localize the inter-domain interface. Residues forming the binding pocket are indicated with *Dashed Lines*. Hinge regions between the NADP- and FAD-binding domains are shown with a *Blue Square* below the x-axis. *Circles* mark the regions of high correlation values between the interface NADP-FAD domains and the binding pocket observed in the correlation map of WT PAMO.